ACS Energy LETTERS

http://pubs.acs.org/journal/aelccp

Physical Model for the Current–Voltage Hysteresis and Impedance of Halide Perovskite Memristors

Mariana Berruet, José Carlos Pérez-Martínez, Beatriz Romero, Cedric Gonzales, Abdullah M. Al-Mayouf, Antonio Guerrero, and Juan Bisquert*

Cite This: ACS Energy Lett. 2022, 7, 1214–1222

Read Online

ACCESS | Metrics & More | Article Recommendations | Supporting Information

ABSTRACT: An investigation of the kinetic behavior of $MAPbI_3$ memristors shows that the onset voltage to a high conducting state depends strongly on the voltage sweep rate, and the impedance spectra generate complex capacitive and inductive patterns. We develop a dynamic model to describe these features and obtain physical insight into the coupling of ionic and electronic properties that produce the resistive switching behavior. The model separates the memristive response into distinct diffusion and transition-state-formation steps that describe well the experimental current–voltage curves at different scan rates and impedance spectra. The ac impedance analysis shows that the halide perovskite memristor response contains the composition of two inductive processes that provide a huge negative capacitance associated with inverted hysteresis. The results provide a new approach to understand some typical characteristics of halide perovskite devices, such as the inductive behavior and hysteresis effects, according to the time scales of internal processes.

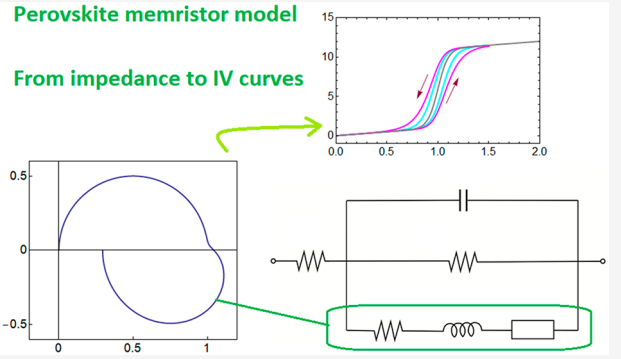

In less than a decade, metal halide perovskite (MHP) materials have established a new photovoltaic (PV) technology that demonstrated very large solar energy conversion efficiencies with low-cost, solution-processed materials.[1−4] The MHP can be described as ABX_3 where A is a monovalent cation such as methylammonium (MA), formamidinium (FA), or cesium (Cs); B is a divalent cation such as lead (Pb) or tin (Sn); and X is a halide anion, including chloride (Cl), bromide (Br), and iodide (I). MHP semiconductors show mixed ionic–electronic conduction in which a significant ionic conductivity due to vacancy displacements exists in addition to the electronic photoconductivity.[5−8] These properties are difficult to measure because of the intersection of very different time scales of ionic and electronic effects that interact with each other. They cause intrinsic memory effects (hysteresis) in current–voltage (I–V)[9−14] that lead to substantial differences in the forward and reverse scan currents and permanent resistive changes. These features are highly significant for important new applications in which MHPs are used for non-optoelectronic applications related to memory storage and brain-like computation. Herein, on the basis of previous understanding of the MHP solar cells,[9,15] we develop a physical model to describe the results of MHP memristors in both voltage cycling and impedance spectroscopy.

A memristor is a two-terminal device whose resistance depends on the history of current and voltage applied to the device. Memristors allow the storage of information by metastable modification of device conductivity.[16−20] Typically, a memristor makes a transition from a high to a low resistance state (HRS–LRS) when a certain threshold forward voltage is passed, which can be restored to the initial state by a reverse voltage sweep.[18,21,22] There has been rapid recent progress in perovskite memristor endurance performance[23] that facilitates application to resistive RAM.[24] Synaptic plasticity, the ability of the connection between neurons to strengthen or weaken by external stimulation, is a central property in the operation of neuronal circuits. The development of spiking neural networks requires a precise control of the functionality of synapses,

Received: January 17, 2022
Accepted: February 23, 2022

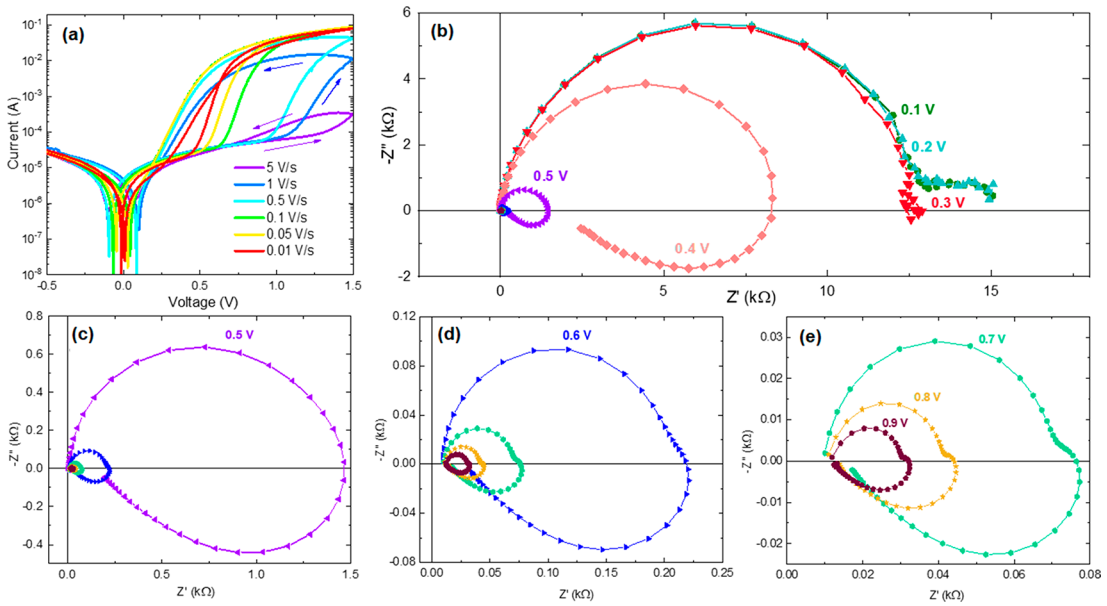

Figure 1. (a) Current−voltage characteristic for an FTO/PEDOT:PSS/MAPI/Au memristor device at 6 different scan rates starting from 5 V/s. Arrows indicate sweep direction. (b−e) Complex plane plot representation of the impedance spectra at different applied dc voltage. Panels c, d, and e correspond to a magnification of the scales.

neurons, and their assemblies by the properties of plasticity, adaptation, spiking, and the synchronization of the temporal dynamics and shapes of repetitive spikes and their integration.[25,26] Currently, there is great interest in developing biorealistic elements that contain no internal circuitry.[27] MHP memristors that undergo a relatively slow transition to HRS take a leading role in the search for emulation of brain functions with assemblies of artificial synapse devices[28−30] in neuromorphic computation.[27,31,32] Furthermore, MHPs provide photoactive synapses suitable to artificial vision devices in which the memory effects can be adapted for preprocessing of image data before transfer to the computing unit eliciting a motor response.[33−35]

In order to design material properties for these applications it is necessary to establish the precise properties of time dynamics of memristors and their response and changes under repetitive stimuli at varying frequency. Impedance spectroscopy (IS) consists of the electrical measurement of current-to-voltage of the device at a steady-state potential V by small perturbation at changing angular frequency ω. It is a central technique for the characterization of PV cells and electrochemical devices.[15,36] We have recently shown that a precise connection can be established between the frequency and time domain in the analysis of hysteresis and time transients of PV devices.[9,37] However, memristors with extreme hysteresis effects have so far not been described with IS models that can predict hysteresis and time transient behavior to determine the physical basis for parameters such as the switching speed and the retention time.

Herein, we take a first step in this direction. We analyze the properties of glass/FTO/PEDOT:PSS/$MAPbI_3$/Au perovskite-based memristor devices.[38,39] The details of device preparation are provided in the Supporting Information. Figure 1 shows the characterization in $I-V$ sweeps of a typical threshold resistive switching device where the switching event is confined to one quadrant only.[40] We note that the effective onset of the transition occurs at higher voltage when the potential sweep is at higher scan rate. The device exhibits ON state retention times of $>10^4$ s at a read voltage of 0.5 V (Figure SI1b), rendering them suitable for volatile memory applications (Figure SI1c). At the beginning, the ON state current exponentially decreases but then stabilizes at 38% of the initial value, maintaining an ON/OFF ratio of ∼1 order of magnitude. Voltage-dependent IS response was performed via a sequence of chronoamperometry (CA) measurement for 10 s, subsequently followed by IS with a frequency range of 0.1 MHz to 0.1 Hz. We note that active areas are very large (0.25 cm^2) for memory applications, but this area helps to maximize the impedance response reducing the noise in the low-frequency region. When devices are scaled to areas of $\sim 10^5$ μm^2, the trends of the $I-V$ curves hold, indicating that the main switching mechanism is maintained but the IS response is noisy (Figure SI2). In any case, the model is still useful to extract different properties of other large-area applications such as solar cells or LEDs.

Figure 1b−e shows the impedance spectra at different applied voltage from 0.1 to 0.9 V. At low voltage the device responds with a double RC arc as is found in solar cell perovskite devices.[15] At 0.3 V and higher voltages a large inductor component at low frequency is formed that is also typical of perovskite solar cells at high voltage, which causes a negative capacitance effect.[9,41−43] This feature has been reported before in perovskite memristors.[39] For 0.5 V and higher the crossing of the real axis of the impedance complex plane shows a strong rightward distortion. This last feature has not been described before, but it is highly reproducible as shown in the Supporting Information with the results of another sample (Figure SI3).

We aim to establish the simplest models that can explain the observed properties of IS and current voltage curves at different scan rates, accounting qualitatively for the strong memory effect and resistive switching phenomena. Our model is adapted to those perovskite memristors that show a gradual transition in current−voltage scans so that the change of conductance can be regulated by the voltage amplitude and operation time.[32] These properties allow us to faithfully

https://doi.org/10.1021/acsenergylett.2c00121
ACS Energy Lett. 2022, 7, 1214−1222

replicate the nature of plasticity in synapses.[28] We adopt a method related to the dynamic systems of neurons,[44,45] of the class of fast−slow dynamic models,[46] that describes rather complex phenomena with a relatively simple number of differential equations, like the two-dimensional FitzHugh−Nagumo neuron model.[47] Another famous model of this type is the Hodgkin−Huxley (HH) model.[48] It is four dimensional with a fast variable (the voltage across the cell membrane) and several slow variables that describe the conduction state of a particular voltage-gated ion channel, which can be opened or closed according to the value of the membrane voltage. In the HH model the channel state is described by a continuous function that varies from 0 to 1 and obeys a first-order kinetic equation for the evolution to the voltage-driven equilibrium state.[44,49] We will utilize this type of state variable in our model as well. In the following paragraphs, we develop the main model and several simplified cases. The expressions and properties are listed in Tables 1, 2, and 3.

Table 1. Main Equations of This Work

equation
$I_{tot} = C_m\frac{du}{dt} + \frac{u}{R_b} + i_c$ (1)
$\tau_d\frac{di_c}{dt} = i_{c0}f - i_c$ (2)
$\frac{df}{dt} = k_0(1-f) - k_1 f$ (3)
$f(u) = \frac{1}{1+e^{-(u-V_T)/V_m}}$ (4)
$\tau_k\frac{df}{dt} = e^{\alpha(u-V_T)/V_m}(1-f) - e^{(\alpha-1)(u-V_T)/V_m}f$ (5)
$\tau_d\frac{di_c}{dt} = i_{c0}\frac{1}{1+e^{-(u-V_T)/V_m}} - i_c$ (6)
$I_{tot} = C_m\frac{du}{dt} + \frac{u}{R_b} + i_{c0}f$ (7)
$I_{tot} = C_m\frac{du}{dt} + qN\frac{df}{dt} + \frac{u}{R_b} + i_{c0}f$ (8)
$I_{tot} = C_m\frac{du}{dt} + qN\frac{df}{dt} + \frac{u}{R_b} + i_c$ (9)

Table 2. Impedance Spectroscopy Models of This Work

equation	figure
$Z(s) = \left[C_m s + {R_b}^{-1} + \frac{1}{Z_c}\right]^{-1}$ (10)	3e
$Z_c(s) = (1+s\tau_d)(R_a + L_a^k s)$ (11)	
$R_a^{-1} = \frac{di_c}{du} = \frac{i_{c0}}{V_m}f(1-f)$ (12)	
$L_a^k = f\tau_k R_a$ (13)	
$L_a^d = \tau_d R_a$ (14)	
$Z_c(\omega) = R_a + i\omega L_a^k + i\omega L_a^d + R_c(\omega)$ (15)	
$R_c(\omega) = -\frac{L_a^k L_a^d}{R_a}\omega^2$ (16)	
$Z(s) = \left[C_m s + {R_b}^{-1} + \frac{1}{R_a + L_a s}\right]^{-1}$ (17)	3a
$Z(s) = \left[C_m s + {R_b}^{-1} + \frac{1}{R_a + L_a^k s} + \frac{1}{R_2 + \frac{1}{C_2 s}}\right]^{-1}$ (18)	3c
$R_2 = \frac{L_a^k i_{c0}}{Q_m}$ (19)	
$C_2 = \frac{Q_m}{R_a i_{c0}}$ (20)	
$Z(s) = \left[C_m s + {R_b}^{-1} + \frac{1}{R_2 + \frac{1}{C_2 s}} + \frac{1}{Z_c}\right]^{-1}$ (21)	SI8

Table 3. Different Models of This Work

denomination	variables	time constants	dynamic equations	impedance function
(1) full transition model	u, i_c, f	τ_m, τ_d, $f\tau_k$	1, 2, 5	9
(2) diffusion-limited	u, i_c	τ_m, τ_d	1, 6	16, $L_a = L_a^d$
(3) formation-limited	u, f	τ_m, $f\tau_k$	7, 5	16, $L_a = L_a^k$
(4) formation and capacitance	u, f	τ_m, $f\tau_k$, τ_2	8, 5	17
(5) inductors and capacitance	u, i_c, f	τ_m, τ_d, $f\tau_k$, τ_2	9, 2, 5	21

The models we propose describe the evolution of the external variables of the MHP memristor, namely, the total current I_{tot} and the voltage across the internal contacts, u, under a certain stimulus out of equilibrium, influenced by two internal variables, i_c and f, that obey the set of dynamic equations (eqs 1−3) indicated in Table 1. These equations define model 1 in Table 3. In this model, we adopt a number of premises to describe the experimental observations. The total current I_{tot} has three components, as indicated in eq 1: a capacitive charging of the interfaces with capacitance C_m, a small ohmic current of constant resistance R_b, and a slow-responding current i_c, with a large saturation value i_{c0}. Very different mechanisms for the formation of the LRS have been suggested in the literature, according to different materials and configurations: (1) formation of a filamentary conductive pathway,[18] (2) decrease of a surface barrier by ion-assisted electrochemical interactions between the perovskite and contacts,[38,50] and (3) decrease of the surface barrier by formation of ion-assisted self-doped regions in the vicinity of interfaces.[27] These physical transformations are often associated with general ion migration effects. In this work, we do not attempt to clarify the mechanism of the investigated memristor, which requires an in-depth investigation of materials and contact properties that will be presented elsewhere. However, in order to describe the complex dynamic properties that have been observed by voltammetry and IS, we will separate clearly two features in the transition to the LRS:

(a) The onset of conduction in quasi-equilibrium depends on a threshold voltage V_T connected to the material properties (bulk and interface). The activation of the high current component i_c occurs by the change of an occupation function $0 \le f \le 1$ that is controlled by the voltage. Similar to the ion channel behavior in neurons, the variable f indicates the state of the mechanism that establishes the high-conductivity state up to the limiting current i_{c0}. Equation 3 is a reaction equation with rate constants k_0 and k_1 that describes the voltage-controlled activation of the high-conduction configuration.

https://doi.org/10.1021/acsenergylett.2c00121
ACS Energy Lett. 2022, 7, 1214−1222

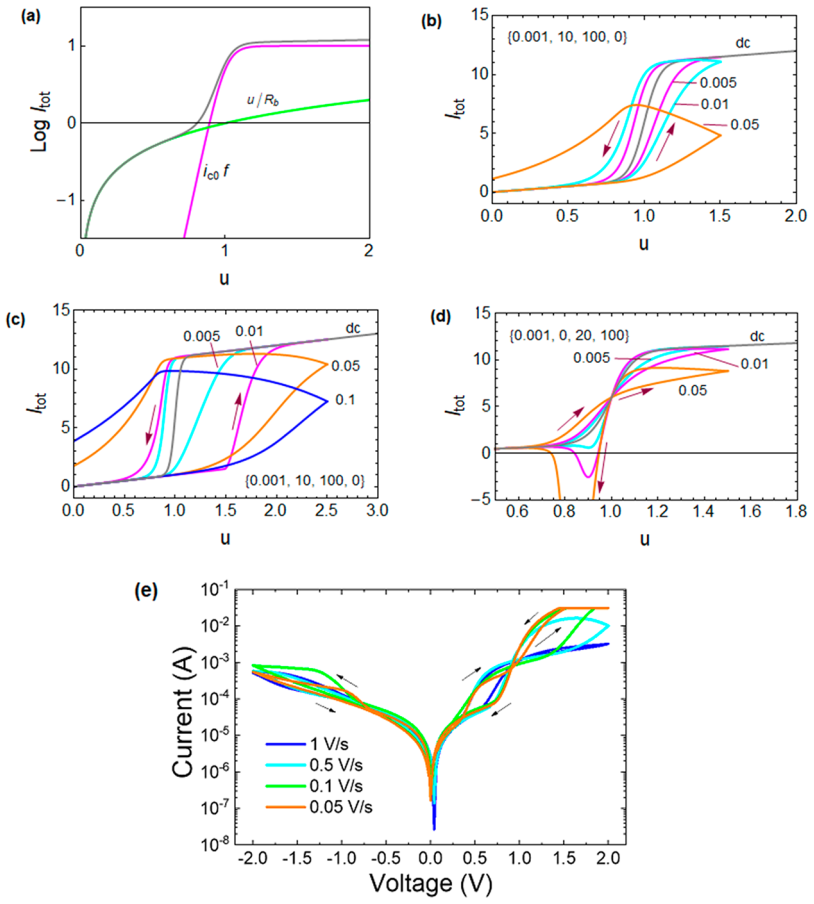

Figure 2. (a) Logarithmic current−voltage curve for model 1 memristor. The gray line is the total equilibrium dc current. (b) Current at forward and backward scan of model 1 at different rates as indicated, $\alpha = 0$, $V_m = 0.05$, and (c) $\alpha = 0.1$, $V_m = 0.025$. Parameters $R_b = 1$; $i_{c0} = 10$, $V_T = 1$, $[\tau_m, \tau_d, \tau_k, Q_m]$. (d) Current at forward and backward scan for model 4 at different rates as indicated, $\alpha = 0$, $V_m = 0.05$, $[\tau_m, \tau_d, \tau_k, Q_m]$. (e) Current−voltage characteristic for an FTO/PEDOT:PSS/MAPI/Spiro-MeOTAD/Au device at 4 different scan rates.

(b) The observations indicate that the increase of f is also determined by the rate of ion transport. We introduce in eq 2 a delay of i_c with the characteristic time τ_d (eq 2). Typically, this temporal parameter represents a diffusion or migration time of ions, necessary to establish the configuration of high f that produces the large electronic current i_{c0}.

This model is an extension of the two-dimensional models that have been recently proposed to describe inductive behavior and inverted hysteresis in MHP and in neurons,[9,15,45,51] and it is also an extension of the standard set of equations for a voltage-controlled memristor.[19,52] Model 1 of eqs 1−3 is three-dimensional and displays additional kinetic complexity that is necessary to account for the observed experimental behaviors of the memristor. We remark that eq 2 is a rather simplified transport equation, and one may use drift-diffusion approaches in a more sophisticated treatment. In addition, the form of eq 3 is not unique but may depend strongly on the kinetics mechanisms and material properties, e.g., with higher-order reaction kinetics. Here we adopt eqs 2 and 3 as the simplest reasonable assumption that illustrates the coupling of different steps in the overall model.

Let us analyze in more detail the properties of the dynamic model. It is important to find, first of all, the steady-state characteristics represented by current−voltage curves. By suppressing the time derivatives in eqs 1−3, we obtain the following conditions for a stationary state:

$$I_{tot} = \frac{u}{R_b} + i_c \tag{22}$$

$$i_c = i_{c0} f \tag{23}$$

$$k_0(1 - f) = k_1 f \tag{24}$$

The last equation can be stated

$$f(u) = \frac{1}{1 + \frac{k_1}{k_0}} \tag{25}$$

By the detailed balance principle, this last equation corresponds to the equilibrium occupancy given by the Fermi−Dirac or Nernst equilibrium distribution function, eq 4, where V_T is the redox potential of the activation state so that in the equilibrium line $f(V_T) = 0.5$. V_m in eq 4 is a constant with dimension of voltage, with a diode ideality factor m with respect to the thermal voltage $k_B T/q$, where T is the absolute temperature, k_B the Boltzmann constant, and q the elementary charge, so that $V_m = mk_B T/q$. Therefore, we obtain

$$\frac{k_0}{k_1} = e^{(u - V_T)/V_m} \tag{26}$$

We introduce the kinetic time of the formation process τ_k. Then the reaction kinetic constants are expressed by a partition that satisfies eq 26:[53]

https://doi.org/10.1021/acsenergylett.2c00121
ACS Energy Lett. 2022, 7, 1214−1222

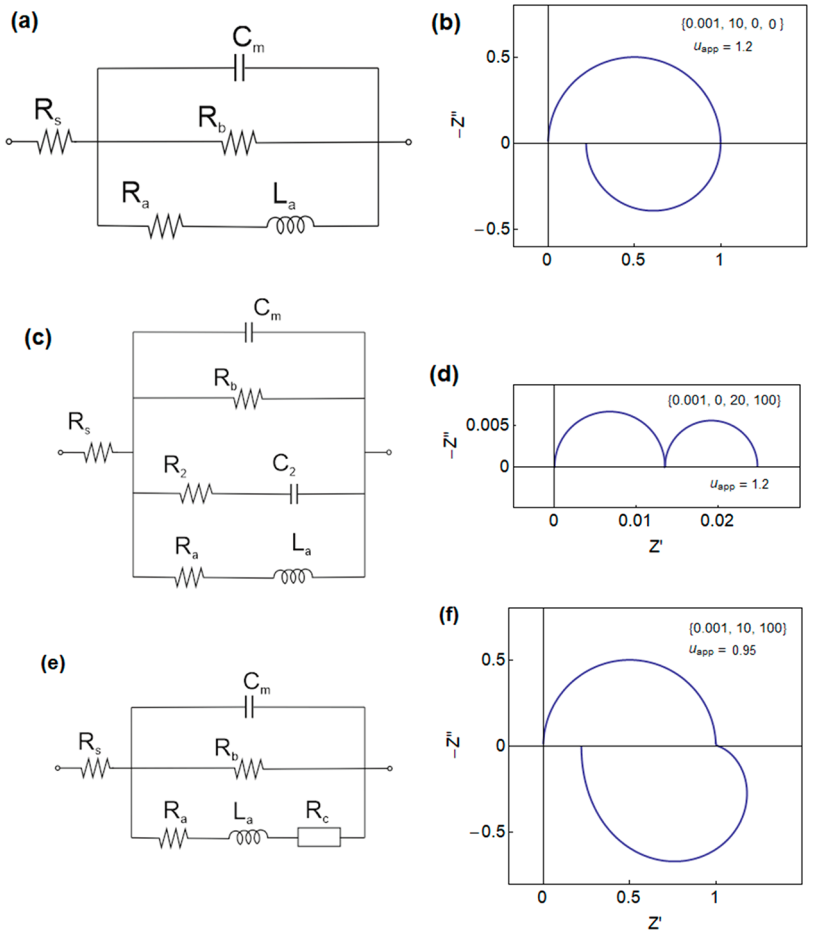

Figure 3. (a) Equivalent circuit model for diffusion-limited model 2 and formation-limited model 3. (b) Impedance spectrum of model 2 for parameters R_b = 1; i_{c0} = 10; V_T = 1; α = 0; V_m = 0.05; [τ_m, τ_d, τ_k, Q_m]. (c) Equivalent circuit model for surface capacitive model 4. (d) Impedance spectrum of model 4. (e) Equivalent circuit model for model 1. (f) Impedance spectrum of model 1.

$$k_0 = \tau_k^{-1} e^{\alpha(u-V_T)/V_m} \tag{27}$$

$$k_1 = \tau_k^{-1} e^{(\alpha-1)(u-V_T)/V_m} \tag{28}$$

The constant $0 \leq \alpha \leq 1$ is a Tafel coefficient. We can write the dynamic eq 3 in the final form (eq 5). In the simulations the unit of time is s, voltage is V, current is A, and resistance is Ω. The steady-state current−voltage equation is

$$I_{app} = \frac{u_{app}}{R_b} + \frac{1}{1 + e^{-(u_{app}-V_T)/V_m}} i_{c0} \tag{29}$$

This is shown in Figure 2a. As stated before, the dc current is formed by two components: an ohmic baseline (green) and a large current that is onset at voltage V_T (magenta). This is the typical form of MHP memristors[27] as shown in Figure 1a.

Memristor dynamics are characterized by a rich variety of transient phenomena that our model is intended to describe. These will be determined by the three time parameters of model 1: $\tau_m = R_b C_m$, τ_d, and τ_k, which we assume to be constants. To analyze these questions, we present the results of CV, in which the current is measured under voltage sweep at scan rate ν_r according to the expression

$$V(t) = V_0 + \nu_r t \tag{30}$$

This method reveals the famous hysteresis effects in current−voltage curves of solar cells.[9,54−57] When we apply eq 30, the model eqs 1, 2, and 5 become

$$I_{tot} = \frac{u}{R_b} + i_c + C_m \nu_r \tag{31}$$

$$\tau_d \nu_r \frac{di_c}{du} = i_{c0} f - i_c \tag{32}$$

$$\tau_k \nu_r \frac{df}{du} = e^{\alpha(u-V_T)/V_m}(1-f) - e^{(\alpha-1)(u-V_T)/V_m} f \tag{33}$$

The two differential equations (32 and 33) can be solved with the chosen boundary conditions. In this case we take $f(u = 0) = 0$ and $i_c(u = 0) = 0$. The voltage-dependent $i_c(u)$ is inserted into eq 29. A set of simulation results of model 1 are presented in Figures 2b,c and SI4. The transition to high conduction happens at higher voltage for fast scan rates, as observed experimentally in Figure 1a. Figure 2c shows a wider separation between forward and backward scans due to a modification of α coefficient. Figure SI4g shows the distinctive conductivity levels that provide the synaptic property of the perovskite memristors by gradual analog switching.[32] The model is valid for both volatile and nonvolatile memories as noted in Figure SI4.

To better understand the dynamic properties, we develop the method of IS. We apply a small perturbation procedure to

https://doi.org/10.1021/acsenergylett.2c00121
ACS Energy Lett. 2022, 7, 1214−1222

the dynamic equations and Laplace-transform the time derivative to $s = i\omega$. The small amplitudes of the variables are denoted $\hat{x}$. The resulting equations have the form

$$\hat{I}_{tot} = \frac{\hat{u}}{R_b} + \hat{i}_c + C_m s\hat{u} \tag{34}$$

$$\tau_d s\hat{i}_c = i_{c0}\hat{f} - \hat{i}_c \tag{35}$$

$$\tau_k s\hat{f} = -\frac{\hat{f}}{f} - \frac{f(1-f)}{V_m}\hat{u} \tag{36}$$

We calculate the impedance $Z(s) = \hat{u}(s)/\hat{I}_{tot}(s)$ and we obtain eqs 10 and 11 where R_a in eq 12 is a resistance and L_a^k and L_a^d are inductors (eqs 13 and 14). These elements have been explained in two-dimensional models in previous publications[15,51] in relation with negative capacitance and hysteresis in MHP. However, model 1 is three-dimensional and contains two inductive processes that are combined in eq 11. This impedance introduces the two inductor elements in the expression of eq 15 and furthermore introduces a negative and frequency-dependent resistance $R_c(\omega)$, eq 16, not previously reported in the literature, to our knowledge. As the standard time constant of the RL elements is R/L, the effective time constants of the model-determining transient behaviors are τ_m, τ_d, $L_a^k/R_a = f\tau_k$. Note that $L_a^k/R_a = \tau_k$ occurs only when $f \approx 1$. The circuit elements and time constants are shown in Figure SI5.

To facilitate a physical interpretation of model 1 we consider simplified cases. We can define conditions in which the reaction time $\tau_k \approx 0$ so that f takes the equilibrium value of eq 4 at any moment. Then eq 2 can be simplified to eq 6 and the dynamic system becomes two-dimensional, with the variables u, i_c, formed by eqs 1 and 6. This can be termed *diffusion-limited transition*, model 2 in Table 3, by analogy to classical electrochemistry terminology.[58] Another limiting situation is when $\tau_d \approx 0$ so that eq 1 can be written as eq 7. Then the dynamic system is two-dimensional also, formed by eqs 7 and 5 with the variables u and f. This is a *formation-limited transition* mechanism, model 3.

By suppressing either τ_d or τ_k in the general impedance of eq 10, the impedance in eq 10 reduces to eq 17 that contains an inductor−resistor branch, as shown in the EC of Figure 3a. This circuit has been well-described before in relation to inverted hysteresis in perovskite solar cells.[9,15,59] The shape of the spectra are shown in Figures 3b and SI6. In the CV behavior we obtain that all models 1, 2, and 3 show inductive or "inverted" hysteresis[10−14] (see Figures 2b,c and SI4c−f). The diffusion-limited model 2 produces a separation of forward and voltage curves right at the onset of the transition, leading to a shift of the effective onset voltage (Figure SI4e). On the other hand, for the formation-limited model 3 in Figure 3d the hysteresis effect occurs only when the current takes a large value (Figure SI4f).

While the large inverted hysteresis is the ordinary behavior of CV of memristors, there are also cases of perovskite memristors with regular hysteresis corresponding to capacitive response.[60,61] To account for such behavior we introduce in eq 1 the capacitive current of the interfacial transition mechanism, $qN\,df/dt$, where N is the total number of surface sites for ions, and the total possible surface charge is $Q_m = Nq$. The resulting equation is indicated in eq 8, and the impedance response is given by eq 18. The EC is presented in Figure 3c. The C_2 in eq 20 is the surface capacitance associated with the activation of interface sites, in addition to the background capacitance C_m, and R_2 in eq 19 is the associated series resistance. The time constant is $\tau_2 = R_2C_2 = L_a^k/R_a$. When $f = 1$, it is $\tau_2 = \tau_k$ by eq 13. This type of serial process at intermediate frequencies has been previously observed unambiguously by Ravishankar et al. in IMPS measurements of $MAPbBr_3$ solar cells,[62] and it was interpreted as an ion accumulation process. The impedance spectra show a regime of two capacitive arcs, Figure 3d, and the inductive element becomes active at large voltage. Consequently, the hysteresis under voltage sweep changes from normal to inverted as shown in Figure 2d. Here we obtain this feature experimentally by introduction of a Spiro-MeOTAD layer as shown in Figure 2e. The crossing of the line in the CV is also observed in the slow scan of Figure 1, indicating the significance of the capacitive contribution at low voltage. Finally, when the Q_m is large the CV becomes fully regular (capacitive) as seen in Figure SI4h. A related two-capacitor circuit is shown in Figure SI10 with the spectra in Figure SI11.

The dominance of RC elements at low voltage and the inductive response at higher voltage can be explained by the increase of the inductive time constant $f\tau_k$ after the transition region, when f increases. However, the simplified models do not accurately describe the impedance spectra at high voltage. We therefore analyze the impedance of model 1 without simplifications. The novelty in this model with respect to the standard circuit of Figure 3a is the product of two $R-L$ impedances in Z_c (eq 11). The full EC is shown in Figure 3e. The simulations of the impedance spectra are shown in Figures 3f and SI7. These and other spectra for different combinations of parameters can be visualized with a Mathematica program presented in the Supporting Information. In the low-voltage region of Figure SI7b the impedance is a single RC arc. As we approach the transition region of the $I-u$ curve, in Figure SI5c the impedance develops the inductive loop already described in Figure 3b. But Figure 3f shows a new type of spectrum not found in the previous models. The behavior caused by the impedance Z_c in the inductive branch increases the real part of the impedance before entering the fourth quadrant. This property corresponds to the high-voltage experimental spectra in Figure 1.

If we turn to the experimental results of Figures 1 and SI2, we note that they show a capacitive response with one of two arcs at low voltage and the generation of an inductive component close to the onset of the current rise. Therefore, we combine all the previous models into model 5 (Table 3) that contains two inductive and two capacitive processes, as shown in Figure SI8, as the minimal model needed for the measured memristors (see the predicted spectral shapes in Figure SI9). A full analysis of the spectral data shows that the impedance model fits well the experimental spectra (Figure SI12) and provides the required parameters (Figures SI13 and SI14). The fitting method is described in the Supporting Information, and it includes the use of constant phase element exponents to account for nonperfect semicircles.[63] An important property of the model is the description of a saturation current in agreement with the experimental results. By the shape of CVs, it is expected that the resistance R_a decreases to a minimum value when $f \approx 1/2$ as indicated in Figure SI5. This is confirmed by the impedance parameters, because the measured R_a decreases exponentially with a diode factor $m = 3.6$ and then undergoes a saturation at large voltage (Figure SI13). The

https://doi.org/10.1021/acsenergylett.2c00121
ACS Energy Lett. 2022, 7, 1214−1222

effective time constants resulting from the impedance spectra fittings are shown in Figure SI15. In the current transition region they are reasonably constant, as assumed in the model. We observe that the longest time is for the kinetic formation of the high conduction effect; hence, the system is predominantly formation-limited, while the ion supply is rather fast in comparison.

The models presented in this work are designed to account for the combination of internal processes in MHP memristors. Our $MAPbI_3$ memristors are admittedly slow, with characteristic times of 10 ms−1 s. The model, however, can be applied to much faster time scales with adequate experimental tools and the specific functions for diffusion and formation characteristics that each case may require. Recently, perovskite memristors for high switching speed with times of 20 ns have been reported by Park et al.[64] From the measurement at different duration pulses, we observe that the resistance for Park et al. is larger for the larger duration pulse, in agreement with our model. Therefore, we believe that the model has a general significance for the analysis of the behavior of memristors, even though we do not claim a universal model because there is a wide variety of materials and systems, and a larger investigation is needed.

In conclusion, we presented the results of kinetic measurements of $MAPbI_3$-based memristors, and we developed a three-dimensional dynamic model that describes well the observed properties of voltage cycling and impedance spectroscopy. The different couplings of ionic and electronic phenomena are characterized by capacitive and inductive features that generate new impedance functions in agreement with the experimental measurements. We also describe well the changes from regular to inverted hysteresis by the dominance of capacitive or inductive elements, respectively. It is not possible to know the formation or diffusion mechanisms a priori, but the essential progress we provide here is the need to separate them, finding the consequences of their compositions on experimental measurements.

■ ASSOCIATED CONTENT

Supporting Information

The Supporting Information is available free of charge at https://pubs.acs.org/doi/10.1021/acsenergylett.2c00121.

Materials and device preparation; details of models; impedance spectra fitting resources and results; Mathematica program to represent current−voltage curves and impedance spectra (PDF)

■ AUTHOR INFORMATION

Corresponding Author

Juan Bisquert − *Institute of Advanced Materials (INAM), Universitat Jaume I, 12006 Castelló, Spain; Yonsei Frontier Lab, Yonsei University, Seoul 03722, South Korea;* orcid.org/0000-0003-4987-4887; Email: bisquert@uji.es

Authors

Mariana Berruet − *Institute of Advanced Materials (INAM), Universitat Jaume I, 12006 Castelló, Spain; División Electroquímica Aplicada, INTEMA, CONICET, Universidad Nacional de Mar del Plata, B7606BWV Mar del Plata, Argentina*

José Carlos Pérez-Martínez − *Institute of Advanced Materials (INAM), Universitat Jaume I, 12006 Castelló, Spain; Electronic Technology Area, Universidad Rey Juan Carlos, 28933 Móstoles, Spain*

Beatriz Romero − *Electronic Technology Area, Universidad Rey Juan Carlos, 28933 Móstoles, Spain*

Cedric Gonzales − *Institute of Advanced Materials (INAM), Universitat Jaume I, 12006 Castelló, Spain;* orcid.org/0000-0002-6550-2007

Abdullah M. Al-Mayouf − *Electrochemical Sciences Research Chair (ESRC), Chemistry Department, College of Science, King Saud University, Riyadh 11451, Saudi Arabia;* orcid.org/0000-0001-9246-7684

Antonio Guerrero − *Institute of Advanced Materials (INAM), Universitat Jaume I, 12006 Castelló, Spain;* orcid.org/0000-0001-8602-1248

Complete contact information is available at: https://pubs.acs.org/10.1021/acsenergylett.2c00121

Notes

The authors declare no competing financial interest.

■ ACKNOWLEDGMENTS

We acknowledge the financial support from Generalitat Valenciana for a Grisolia grant (GRISOLIAP/2019/048) and Ministerio de Ciencia y Innovación (PID2019-107348GB-100). We also acknowledge the financial support of CONICET (Extern Fellowship 2020); Comunidad de Madrid (S2018/NMT-4326-SINFOTON2-CM); and Universidad Rey Juan Carlos "Grupo DELFO de alto rendimiento", reference M2363, under research program "Programa de fomento y desarrollo de la investigación".

■ REFERENCES

(1) Kojima, A.; Teshima, K.; Shirai, Y.; Miyasaka, T. Organometal halide perovskites as visible-light sensitizers for photovoltaic cells. *J. Am. Chem. Soc.* **2009**, *131*, 6050−6051.

(2) *Organic-Inorganic Halide Perovskite Photovoltaics: From Fundamentals to Device Architectures*; Park, N.-G., Grätzel, M., Miyasaka, T., Eds.; Springer, 2016.

(3) Nayak, P. K.; Mahesh, S.; Snaith, H. J.; Cahen, D. Photovoltaic solar cell technologies: analysing the state of the art. *Nat. rev. Mater.* **2019**, *4*, 269−285.

(4) Kim, J. Y.; Lee, J.-W.; Jung, H. S.; Shin, H.; Park, N.-G. High-Efficiency Perovskite Solar Cells. *Chem. Rev.* **2020**, *120*, 7867−7918.

(5) Azpiroz, J. M.; Mosconi, E.; Bisquert, J.; De Angelis, F. Defect migration in methylammonium lead iodide and its role in perovskite solar cell operation. *Energy Environ. Sci.* **2015**, *8*, 2118−2127.

(6) Senocrate, A.; Maier, J. Solid-State Ionics of Hybrid Halide Perovskites. *J. Am. Chem. Soc.* **2019**, *141*, 8382−8396.

(7) Lopez-Varo, P.; Jiménez-Tejada, J. A.; García-Rosell, M.; Ravishankar, S.; Garcia-Belmonte, G.; Bisquert, J.; Almora, O. Device Physics of Hybrid Perovskite Solar cells: Theory and Experiment. *Adv. Energy Mater.* **2018**, *8*, 1702772.

(8) Zhang, T.; Hu, C.; Yang, S. Ion Migration: A "Double-Edged Sword" for Halide-Perovskite-Based Electronic Devices. *Small Methods* **2020**, *4*, 1900552.

(9) Bisquert, J.; Guerrero, A.; Gonzales, C. Theory of Hysteresis in Halide Perovskites by Integration of the Equivalent Circuit. *ACS Phys. Chem. Au* **2021**, *1*, 25−44.

(10) Almora, O.; Aranda, C.; Zarazua, I.; Guerrero, A.; Garcia-Belmonte, G. Noncapacitive Hysteresis in Perovskite Solar Cells at Room Temperature. *ACS Energy Lett.* **2016**, *1*, 209−215.

(11) Rong, Y. G.; Hu, Y.; Ravishankar, S.; Liu, H. W.; Hou, X. M.; Sheng, Y. S.; Mei, A. Y.; Wang, Q. F.; Li, D. Y.; Xu, M.; Bisquert, J.; Han, H. W. Tunable hysteresis effect for perovskite solar cells. *Energy Environ. Sci.* **2017**, *10*, 2383−2391.

(12) Tress, W.; Correa Baena, J. P.; Saliba, M.; Abate, A.; Graetzel, M. Inverted Current−Voltage Hysteresis in Mixed Perovskite Solar Cells: Polarization, Energy Barriers, and Defect Recombination. *Adv. Energy Mater.* **2016**, *6*, 1600396.
(13) Wu, F.; Pathak, R.; Chen, K.; Wang, G.; Bahrami, B.; Zhang, W.-H.; Qiao, Q. Inverted Current−Voltage Hysteresis in Perovskite Solar Cells. *ACS Energy Lett.* **2018**, *3*, 2457−2460.
(14) Alvarez, A. O.; Arcas, R.; Aranda, C. A.; Bethencourt, L.; Mas-Marzá, E.; Saliba, M.; Fabregat-Santiago, F. Negative Capacitance and Inverted Hysteresis: Matching Features in Perovskite Solar Cells. *J. Phys. Chem. Lett.* **2020**, *11*, 8417−8423.
(15) Guerrero, A.; Bisquert, J.; Garcia-Belmonte, G. Impedance spectroscopy of metal halide perovskite solar cells from the perspective of equivalent circuits. *Chem. Rev.* **2021**, *121*, 14430−14484.
(16) Kwak, K. J.; Lee, D. E.; Kim, S. J.; Jang, H. W. Halide Perovskites for Memristive Data Storage and Artificial Synapses. *J. Phys. Chem. Lett.* **2021**, *12*, 8999−9010.
(17) Kang, K.; Hu, W.; Tang, X. Halide Perovskites for Resistive Switching Memory. *J. Phys. Chem. Lett.* **2021**, *12*, 11673−11682.
(18) Fang, Y.; Zhai, S.; Chu, L.; Zhong, J. Advances in Halide Perovskite Memristor from Lead-Based to Lead-Free Materials. *ACS Appl. Mater. Int.* **2021**, *13*, 17141−17157.
(19) Pershin, Y. V.; Di Ventra, M. Memory effects in complex materials and nanoscale systems. *Adv. Phys.* **2011**, *60*, 145−227.
(20) Rahimi Azghadi, M.; Chen, Y.-C.; Eshraghian, J. K.; Chen, J.; Lin, C.-Y.; Amirsoleimani, A.; Mehonic, A.; Kenyon, A. J.; Fowler, B.; Lee, J. C.; Chang, Y.-F. Complementary Metal-Oxide Semiconductor and Memristive Hardware for Neuromorphic Computing. *Advanced Intelligent Systems* **2020**, *2*, 1900189.
(21) Gogoi, H. J.; Bajpai, K.; Mallajosyula, A. T.; Solanki, A. Advances in Flexible Memristors with Hybrid Perovskites. *J. Phys. Chem. Lett.* **2021**, *12*, 8798−8825.
(22) Zhao, X.; Xu, H.; Wang, Z.; Lin, Y.; Liu, Y. Memristors with organic-inorganic halide perovskites. *InfoMat* **2019**, *1*, 183−210.
(23) Poddar, S.; Zhang, Y.; Gu, L.; Zhang, D.; Zhang, Q.; Yan, S.; Kam, M.; Zhang, S.; Song, Z.; Hu, W.; Liao, L.; Fan, Z. Down-Scalable and Ultra-fast Memristors with Ultra-high Density Three-Dimensional Arrays of Perovskite Quantum Wires. *Nano Lett.* **2021**, *21*, 5036−5044.
(24) Kim, H.; Han, J. S.; Kim, S. G.; Kim, S. Y.; Jang, H. W. Halide perovskites for resistive random-access memories. *J. Mater. Chem. C* **2019**, *7*, 5226−5234.
(25) Zamarreño-Ramos, C.; Serrano-Gotarredona, T.; Camuñas-Mesa, L.; Perez-Carrasco, J.; Masquelier, T.; Linares-Barranco, B. On Spike-Timing-Dependent-Plasticity, Memristive Devices, and Building a Self-Learning Visual Cortex. *Frontiers Neuroscience* **2011**, *5*, 26.
(26) Covi, E.; Brivio, S.; Serb, A.; Prodromakis, T.; Fanciulli, M.; Spiga, S. Analog Memristive Synapse in Spiking Networks Implementing Unsupervised Learning. *Front. Neurosci.* **2016**, *10*, 482.
(27) John, R. A.; Yantara, N.; Ng, S. E.; Patdillah, M. I. B.; Kulkarni, M. R.; Jamaludin, N. F.; Basu, J.; Ankit; Mhaisalkar, S. G.; Basu, A.; Mathews, N. Diffusive and Drift Halide Perovskite Memristive Barristors as Nociceptive and Synaptic Emulators for Neuromorphic Computing. *Adv. Mater.* **2021**, *33*, 2007851.
(28) Xu, W.; Cho, H.; Kim, Y.-H.; Kim, Y.-T.; Wolf, C.; Park, C.-G.; Lee, T.-W. Organometal Halide Perovskite Artificial Synapses. *Adv. Mater.* **2016**, *28*, 5916−5922.
(29) Xiao, Z.; Huang, J. Energy-Efficient Hybrid Perovskite Memristors and Synaptic Devices. *Adv. Electron. Mater.* **2016**, *2*, 1600100.
(30) Christensen, D. V.; Dittmann, R.; Linares-Barranco, B.; Sebastian, A.; Le Gallo, M. 2022 roadmap on neuromorphic computing and engineering, *Neuromorphic Computing and Engineering* **2022**. DOI: 10.1088/2634-4386/ac4a83
(31) Choi, J.; Han, J. S.; Hong, K.; Kim, S. Y.; Jang, H. W. Organic−Inorganic Hybrid Halide Perovskites for Memories, Transistors, and Artificial Synapses. *Adv. Mater.* **2018**, *30*, 1704002.
(32) Yang, J.-Q.; Wang, R.; Wang, Z.-P.; Ma, Q.-Y.; Mao, J.-Y.; Ren, Y.; Yang, X.; Zhou, Y.; Han, S.-T. Leaky integrate-and-fire neurons based on perovskite memristor for spiking neural networks. *Nano Energy* **2020**, *74*, 104828.
(33) Yang, X.; Xiong, Z.; Chen, Y.; Ren, Y.; Zhou, L.; Li, H.; Zhou, Y.; Pan, F.; Han, S.-T. A self-powered artificial retina perception system for image preprocessing based on photovoltaic devices and memristive arrays. *Nano Energy* **2020**, *78*, 105246.
(34) Kim, M. S.; Kim, M. S.; Lee, G. J.; Sunwoo, S.-H.; Chang, S.; Song, Y. M.; Kim, D.-H. Bio-Inspired Artificial Vision and Neuromorphic Image Processing Devices. *Advanced Materials Technologies* **2022**, *7*, 2100144.
(35) Gong, J.; Wei, H.; Ni, Y.; Zhang, S.; Du, Y.; Xu, W. Methylammonium halide-doped perovskite artificial synapse for light-assisted environmental perception and learning. *Materials Today Physics* **2021**, *21*, 100540.
(36) von Hauff, E. Impedance Spectroscopy for Emerging Photovoltaics. *J. Phys. Chem. C* **2019**, *123*, 11329−11346.
(37) Bisquert, J.; Janssen, M. From Frequency Domain to Time Transient Methods for Halide Perovskite Solar Cells: The Connections of IMPS, IMVS, TPC and TPV. *J. Phys. Chem. Lett.* **2021**, *12*, 7964−7971.
(38) Solanki, A.; Guerrero, A.; Zhang, Q.; Bisquert, J.; Sum, T. C. Interfacial Mechanism for Efficient Resistive Switching in Ruddlesden-Popper Perovskites for Non-Volatile Memories. *J. Phys. Chem. Lett.* **2020**, *11*, 463−470.
(39) Gonzales, C.; Guerrero, A.; Bisquert, J. Spectral properties of the dynamic state transition in metal halide perovskite-based memristor exhibiting negative capacitance. *Appl. Phys. Lett.* **2021**, *118*, 073501.
(40) Lanza, M.; Wong, H. S. P.; Pop, E.; Ielmini, D.; Strukov, D.; Regan, B. C.; Larcher, L.; Villena, M. A.; Yang, J. J.; Goux, L.; Belmonte, A.; Yang, Y.; Puglisi, F. M.; Kang, J.; Magyari-Köpe, B.; Yalon, E.; Kenyon, A.; Buckwell, M.; Mehonic, A.; Shluger, A.; Li, H.; Hou, T.-H.; Hudec, B.; Akinwande, D.; Ge, R.; Ambrogio, S.; Roldan, J. B.; Miranda, E.; Suñe, J.; Pey, K. L.; Wu, X.; Raghavan, N.; Wu, E.; Lu, W. D.; Navarro, G.; Zhang, W.; Wu, H.; Li, R.; Holleitner, A.; Wurstbauer, U.; Lemme, M. C.; Liu, M.; Long, S.; Liu, Q.; Lv, H.; Padovani, A.; Pavan, P.; Valov, I.; Jing, X.; Han, T.; Zhu, K.; Chen, S.; Hui, F.; Shi, Y. Recommended Methods to Study Resistive Switching Devices. *Adv. Electron. Mater.* **2019**, *5*, 1800143.
(41) Zohar, A.; Kedem, N.; Levine, I.; Zohar, D.; Vilan, A.; Ehre, D.; Hodes, G.; Cahen, D. Impedance Spectroscopic Indication for Solid State Electrochemical Reaction in (CH3NH3)PbI3 Films. *J. Phys. Chem. Lett.* **2016**, *7*, 191−197.
(42) Khan, M. T.; Huang, P.; Almohammedi, A.; Kazim, S.; Ahmad, S. Mechanistic origin and unlocking of negative capacitance in perovskites solar cells. *iScience* **2021**, *24*, 102024.
(43) Fabregat-Santiago, F.; Kulbak, M.; Zohar, A.; Vallés-Pelarda, M.; Hodes, G.; Cahen, D.; Mora-Seró, I. Deleterious Effect of Negative Capacitance on the Performance of Halide Perovskite Solar Cells. *ACS Energy Lett.* **2017**, *2*, 2007−2013.
(44) Izhikevich, E. M. *Dynamical Systems in Neuroscience*; MIT Press, 2007.
(45) Bisquert, J. A frequency domain analysis of excitability and bifurcations of Fitzhugh-Nagumo neuron model. *J. Phys. Chem. Lett.* **2021**, *12*, 11005−11013.
(46) Kuehn, C. *Multiple Time Scale Dynamics*; Springer, 2015.
(47) Nagumo, J.; Arimoto, S.; Yoshizawa, S. An Active Pulse Transmission Line Simulating Nerve Axon. *Proceedings of the IRE* **1962**, *50*, 2061−2070.
(48) Hodgkin, A. L.; Huxley, A. F. A quantitative description of membrane current and its application to conduction and excitation in nerve. *J. Physiol* **1952**, *117*, 500−544.
(49) Wallisch, P.; Lusignan, M. E.; Benayoun, M. D.; Baker, T. I.; Dickey, A. S.; Hatsopoulos, N. H. *MATLAB for Neurosciences*; Elsevier, 2014.
(50) Yang, J. J.; Strukov, D. B.; Stewart, D. R. Memristive devices for computing. *Nat. Nanotechnol.* **2013**, *8*, 13−24.

(51) Bou, A.; Bisquert, J. Impedance spectroscopy dynamics of biological neural elements: from memristors to neurons and synapses. *J. Phys. Chem. B* **2021**, *125*, 9934−9949.
(52) Chua, L. Memristor, Hodgkin−Huxley, and Edge of Chaos. *Nanotechnology* **2013**, *24*, 383001.
(53) Bisquert, J. *The Physics of Solar Energy Conversion*; CRC Press: Boca Raton, FL, 2020.
(54) Kang, D.-H.; Park, N.-G. On the Current−Voltage Hysteresis in Perovskite Solar Cells: Dependence on Perovskite Composition and Methods to Remove Hysteresis. *Adv. Mater.* **2019**, *31*, 1805214.
(55) Unger, E. L.; Hoke, E. T.; Bailie, C. D.; Nguyen, W. H.; Bowring, A. R.; Heumuller, T.; Christoforo, M. G.; McGehee, M. D. Hysteresis and transient behavior in current-voltage measurements of hybrid-perovskite absorber solar cells. *Energy Environ. Sci.* **2014**, *7*, 3690−3698.
(56) Snaith, H. J.; Abate, A.; Ball, J. M.; Eperon, G. E.; Leijtens, T.; Noel, N. K.; Stranks, S. D.; Wang, J. T.-W.; Wojciechowski, K.; Zhang, W. Anomalous Hysteresis in Perovskite Solar Cells. *J. Phys. Chem. Lett.* **2014**, *5*, 1511−1515.
(57) Kim, H.-S.; Jang, I.-H.; Ahn, N.; Choi, M.; Guerrero, A.; Bisquert, J.; Park, N.-G. Control of I-V Hysteresis in CH3NH3PbI3 Perovskite Solar Cell. *J. Phys. Chem. Lett.* **2015**, *6*, 4633−4639.
(58) Bard, A. J.; Faulkner, L. R. *Electrochemical Methods, Fundamentals and Applications*, 2nd ed.; John Wiley & Sons: Weinheim, Germany, 2001.
(59) Ghahremanirad, E.; Bou, A.; Olyaee, S.; Bisquert, J. Inductive Loop in the Impedance Response of Perovskite Solar Cells Explained by Surface Polarization Model. *J. Phys. Chem. Lett.* **2017**, *8*, 1402−1406.
(60) Wang, S.; Xiong, Y.; Dong, X.; Sha, J.; Wu, Y.; Li, W.; Wang, Y. Capacitive coupling behaviors based on triple cation organic-inorganic hybrid perovskite memristor. *J. Alloys Compd.* **2021**, *874*, 159884.
(61) Chua, L. Resistance switching memories are memristors. *Appl. Phys. A: Mater. Sci. Process.* **2011**, *102*, 765−783.
(62) Ravishankar, S.; Aranda, C.; Sanchez, S.; Bisquert, J.; Saliba, M.; Garcia-Belmonte, G. Perovskite Solar Cell Modeling Using Light and Voltage Modulated Techniques. *J. Phys. Chem. C* **2019**, *123*, 6444−6449.
(63) Lasia, A. The Origin of the Constant Phase Element. *J. Phys. Chem. Lett.* **2022**, *13*, 580−589.
(64) Park, Y.; Kim, S. H.; Lee, D.; Lee, J.-S. Designing zero-dimensional dimer-type all-inorganic perovskites for ultra-fast switching memory. *Nat. Commun.* **2021**, *12*, 3527.

https://doi.org/10.1021/acsenergylett.2c00121
ACS Energy Lett. 2022, 7, 1214−1222